Journal of Agrosystems and Analytics
Volume 1 Issue 1 2026 (Jan-June 2026) | Page No:- 1-14

RESEARCH ARTICLE

Estimation of Land Surface Heat Fluxes Based on Landsat 8 Satellite Data

V. B. Virani[1]*

[1]Agricultural Meteorological Cell, Navsari Agricultural University, Navsari, Gujarat, India

(*Received 6 January 2026, Accepted 13 March 2026*)

***Corresponding author:** vivekvirani9999@gmail.com

Abstract

Land surface heat fluxes encompass net radiation flux (Rn), soil heat flux (G), sensible heat flux (H), and latent heat flux (LE), all of which play a crucial role in understanding energy transfer within earth–atmosphere interactions. This study utilized Landsat 8 data to estimate land surface heat fluxes over the Navsari district of South Gujarat, India using the SEBAL (Surface Energy Balance Algorithm for Land) model. Rn followed a seasonal trend of summer > autumn > spring > winter, with median values ranging from 607.7 W/m^2 in summer to 459.9 W/m^2 in winter. G exhibited a similar pattern, while H varied as summer > winter > spring > autumn. LE showed the opposite trend, peaking in autumn (427.3 W/m^2) and decreasing through spring, winter, and summer. Notably, the LE remained higher than the H across all seasons. Rn was primarily allocated to LE across most LULC types, except in water bodies, where it was nearly evenly distributed between LE and G. In the absence of ground-based instruments, SEBAL outputs were validated using EEFlux METRIC, a cloud-based evapotranspiration (ET) estimation tool. The validation showed strong agreement for land surface temperature (LST) (R^2 = 0.976, RMSE = 5.63 K) and moderate agreement for ET (R^2 = 0.632, RMSE = 1.40 mm/day), albedo (R^2 = 0.532, RMSE = 0.06), and crop coefficient Kc (R^2 = 0.452, RMSE = 0.18). The SEBAL model was also applied to estimate seasonal ET and determine the total water requirement for sugarcane.

Keywords: SEBAL; Energy Balance; Landsat 8; Sensible Heat Flux; Latent Heat Flux

1. Introduction

Rn represents the total energy available at the land surface, which is subsequently distributed among G, H, and LE. G accounts for the energy absorbed by or conducted into the soil. H refers to the heat transfer between the land surface and the atmosphere due to temperature gradients, while LE represents the energy used for phase changes of water vapor, primarily through ET (Zhang *et al.,* 2016). This partitioning of energy plays a critical role in regulating surface temperature, atmospheric dynamics, and hydrological processes (Wagle *et al.,* 2019). Variations in land surface heat fluxes can result from changes in land use and land cover (LULC), as well as natural fluctuations, making them useful indicators of environmental transformations in both natural and human-modified landscapes (Zhao *et al.,* 2014). Additionally, these fluxes directly influence LST, a key factor contributing to local warming (Zhang *et al.,* 2016). Other contributing factors include urbanization, which alters surface albedo and thermal properties (Peng *et al.,* 2012), deforestation, which impacts surface roughness and energy balance (Lawrence and Vandecar, 2015), and soil moisture variations, which modulate LE and H fluxes (Seneviratne *et al.,* 2010). Furthermore, alterations in land surface heat fluxes can affect atmospheric circulation and climate patterns, emphasizing their importance in understanding energy exchanges in land–atmosphere interactions (Wang *et al.,* 2018).

Several pioneering studies have utilized the SEBAL model to estimate land surface heat fluxes and ET in India using satellite remote sensing data (Singh *et al.,* 2008; Singh *et al.,* 2020; Aryalekshmi *et al.,* 2021; Shukla *et al.,* 2021; Bhattacharya *et al.,* 2022; Karishma *et al.,* 2022; Saxena *et al.,* 2024, and Virani *et al.,* 2024). Aryalekshmi *et al.,* (2021) analyzed various surface energy balance models for estimating evapotranspiration in the Malaprabha River Basin, Karnataka, India. Using

Landsat 8 OLI/TIRS data, they compared SEBAL, METRIC, and S-SEBI models. SEBAL slightly overestimated ET compared to ground data, but all models provided reliable estimates, highlighting their utility for water resource management. Shukla *et al.,* (2021) estimated ET using the SEBS model in Chhatarpur and Panna, Madhya Pradesh, India. They utilized Landsat 8 OLI and Landsat TM data over 20 years. The study highlighted the impact of land use changes on ET, emphasizing its role in water resource management. Saxena *et al.,* (2024) estimated ET in Western Rajasthan, India, using an improvised SEBAL method with Landsat 8 and MODIS data. Their study, conducted via Google Earth Engine (GEE), found SEBAL reliable for large-scale ET estimation, with higher ET in irrigated areas and a declining trend linked to climate change.

2. Study Area and Datasets

2.1 Study area

The present study focuses on Navsari district in Gujarat, India, which is geographically positioned between 20°32' to 21°05' North latitude and 72°42' to 73°30' East longitude (Figure 1). Located in the South Gujarat region, between Surat and Valsad districts, Navsari falls under the South Gujarat heavy rainfall agroclimatic zone, which significantly influences its climate, agriculture, and natural resources. The district spans a total geographical area of 2,204 km² and receives an average annual rainfall of 1,731 mm, based on data from the past three decades. The study area exhibits a diverse LULC pattern, which includes sugarcane cultivation (8.82%), other vegetation (26.22%), bare soil (6.13%), and deciduous forest (13.36%). Additionally, orchard plantations cover 26.02% of the area, while built-up regions account for 10.13%, water bodies for 5.92%, and fallow land represents 3.40% (Figure 1). This detailed LULC distribution plays a significant role in influencing surface energy balance and evapotranspiration patterns across the region.

The IMD weather station, situated at Navsari Agricultural University (NAU), reports an average maximum temperature of 32.11°C and a minimum temperature of 25.5°C. Agriculture is the backbone of the region's economy, with rice and sugarcane being the dominant crops. Additionally, the district is known for its thriving orchard farming, producing banana, mango, and sapota. Navsari also features a significant deciduous forest cover, extending across approximately 274 km², contributing to the region's ecological balance.

2.2 Data

To estimate land surface fluxes (Rn, G, H, and LE) using the SEBAL model, this study integrated space-borne imagery, a Digital Elevation Model (DEM), and ground-based meteorological data. Cloud-free Landsat 8 Collection 2 Level-2 data (path 148/row 46, 30 m resolution)—pre-corrected for atmospheric and radiometric effects (Table 1) via LaSRC and MODTRAN—and SRTM DEM data were acquired from the USGS Earth Explorer. Concurrent meteorological parameters (temperature, wind speed, and relative humidity) were obtained from the Automatic Weather Station (AWS) at NAU, Navsari, to compute instantaneous (mm/hr) and daily (mm/day) reference evapotranspiration (RET). The satellite overpass time (~11:00:54 IST) aligned precisely with the 15-minute recording intervals of the AWS, ensuring excellent temporal synchronization between the satellite and ground-based measurements.

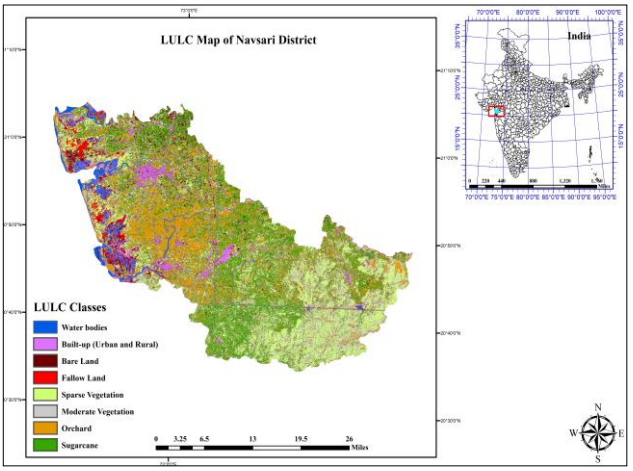

Fig. 1. Land use land cover (LULC) classes of Navsari District, the study area.

Table 1 Details of Landsat 8 data used in the study

Sr. No.	Data Acquisition Date	Scene Specification	Cloud Cover (%)
1	27/10/2022	LC08_L2SP_148046_20221027_20221107_02_T1	0.0
2	28/11/2022	LC08_L2SP_148046_20221128_20221206_02_T1	0.0
3	30/12/2022	LC08_L2SP_148046_20221230_20230110_02_T1	0.0
4	31/01/2023	LC08_L2SP_148046_20230131_20230208_02_T1	0.0
5	16/02/2023	LC08_L2SP_148046_20230216_20230223_02_T1	0.0
6	04/03/2023	LC08_L2SP_148046_20230304_20230316_02_T1	0.2
7	21/04/2023	LC08_L2SP_148046_20230421_20230429_02_T1	0.0
8	24/05/2023	LC08_L2SP_148046_20230523_20230602_02_T1	8.0

3. Methodology

3.1 SEBAL algorithm

The SEBAL algorithm to estimates land surface fluxes using Landsat 8 data by calculating latent heat (LE) as the residual component of the surface energy balance equation (Equation 1). The development of SEBAL is

primarily based on methodologies outlined in the works of Bastiaanssen *et al.,* (1998), Bastiaanssen (2000), Waters (2002), Sun *et al.,* (2011), Silva *et al.,* (2016), Beg *et al.,* (2016), Caiserman *et al.,* (2021), and Virani *et al.,* (2024).

$$\mathbf{LE = R_n - H - G} \quad \textbf{(1)}$$

Where, Rn is the net radiation, G is the soil heat flux and H is the sensible heat flux.
The step-by-step procedure to estimating components of land surface fluxes are given below.

Net radiation (R_n): Net radiation is calculated by deducting the outgoing and incoming longwave radiation components from the incoming shortwave radiation.

$$\mathbf{R_n = R_s\downarrow (1 - \alpha) + R_L\downarrow - R_L\uparrow - (1 - \varepsilon_s) R_L\downarrow} \quad \textbf{(2)}$$

Where, $R_S\downarrow$ represents the incoming shortwave radiation (W/m^2), $R_L\uparrow$ denotes the outgoing longwave radiation (W/m^2), and $R_L\downarrow$ corresponds to the incoming longwave radiation (W/m^2). Additionally, α refers to the surface albedo, while ε_s indicates the surface emissivity.

$$Rs\downarrow = Gsc * \cos\theta * dr * \tau_{sw} \quad \textbf{(2a)}$$

Where, G_{Sc} represents the solar constant (1367 W/m^2), θ is the solar incidence angle ($\theta = 90 - \phi$), and ϕ denotes the solar elevation angle (as provided in the metadata file). The term dr corresponds to the inverse Earth-Sun distance (also available in the metadata file), while τ_{sw} represents the atmospheric transmissivity, calculated using the formula: $\tau_{sw} = 0.75 + (2 \times 10^{-5} \times$ station elevation in meters).

$$R_L\uparrow = \varepsilon_s * \sigma * LST^4 \quad \textbf{(2b)}$$

Where, ε_s represents the surface emissivity (dimensionless), σ is the Stefan–Boltzmann constant (5.67 x 10^{-8} W/m^2 K^{-4}), and LST is land surface temperature (K).

$$\varepsilon_s = 1.009 + 0.047 * \ln (NDVI) \quad \textbf{(2c)}$$

The above relationship is applicable only for NDVI values greater than 0.0. For pixels with NDVI values below 0.0, which typically represent water bodies, an emissivity value of 0.985 was assigned (Waters, 2002).

$$R_L\downarrow = \varepsilon_a * \sigma * T_a \quad \textbf{(2d)}$$

Where, ε_a represents the atmospheric emissivity, calculated as = $0.85(-\ln\tau_{sw})^{0.09}$, and T_a denotes the near-surface air temperature (K).

Surface albedo (α) is determined by first calculating the spectral radiance ($L\lambda$) and spectral reflectance ($\rho\lambda$) at the top of atmosphere (TOA) for each band (bands 2 to 7 for Landsat 8). Subsequently, the TOA albedo (α_{TOA}) is computed using Equation 3.

$$\alpha_{TOA} = \sum (\omega_\lambda * \rho_\lambda) \quad \textbf{(3)}$$

Where, ω_λ represents the constant weighting coefficient for each band (bands 2 to 7).

The computation of the α by following Equation 3a.

$$\alpha = \alpha_{TOA} - \alpha_{path\_radiance} / \tau_{sw}^2 \quad \textbf{(3a)}$$

Where, $\alpha_{path\_radiance}$ represents the average fraction of incoming solar radiation, across all bands, that is backscattered to the satellite before reaching the Earth's surface. The values of $\alpha_{path\_radiance}$ typically range between 0.025 and 0.04.

Ground heat flux (G): It represents the rate of heat storage in the soil due to conduction and is calculated as a function of net radiation, surface albedo, and vegetation cover.

$$G = [LST + 273/\alpha] * [(0.0038\alpha + 0.0074\alpha^2) * (1\ 0.98NDVI^4) * Rn] \quad \textbf{(4)}$$

$$LST = BT / [1 + W * (BT / 14380) * \ln(\varepsilon_s)] \quad \textbf{(4a)}$$

Where, BT represents the brightness temperature at the TOA in Kelvin (K), and W denotes the wavelength of emitted radiance. For Landsat 8 Band 10, W is 10.89 µm.

Sensible heat flux (H): It is referring to the transfer of heat energy between the atmosphere and earth surface through convection due to temperature difference. The sensible heat flux is difficult to calculate because of values of aerodynamic resistance (r_{ah}) and temperature different between two known heights (dT) at each pixel are unknown. The calculation of H follows an iterative process due to the calculation interdependence between $\mathbf{r_{ah}}$ and **H** (Sawadogo *et al.,* 2020).

$$\mathbf{H = \rho_{air} * Cp * dT / r_{ah}} \quad \textbf{(5)}$$

Where, where ρ_{air} is the air density (kg m^{-3}), Cp is the specific heat of air at constant pressure (=1004 J kg^{-1} K^{-1}), dT is the vertical near surface temperature difference (K), and a and b are empirical coefficients (Figure 2).

Initially, the iteration assumes neutral atmospheric conditions, providing a preliminary estimation of **H** under neutral conditions. This estimated **H** is then used to calculate the Monin-Obukhov length (**L**). The SEBAL model applies the Monin-Obukhov theory in its iterative process to account

for atmospheric stability or instability effects on $\mathbf{r_{ah}}$. The iteration adjusts the $\mathbf{r_{ah}}$ value by incorporating stability corrections for momentum and heat transport based on prevailing atmospheric conditions (Waters, 2002), leading to updated **H** values. SEBAL continues this iterative process until the $\mathbf{r_{ah}}$ value stabilizes, meaning that the deviation between successive values is less than 5% for three consecutive iterations (Sawadogo *et al.,* 2020).

The values of the integrated stability corrections for momentum ($\mathbf{\Psi_m}$) and heat transport ($\mathbf{\Psi_h}$) are computed using the formulations by **Paulson (1970)** and **Webb (1970)**, depending on the sign of **L**. When **L < 0**, the lower atmospheric boundary layer is **unstable**, whereas when **L > 0**, the boundary layer is **stable**. The stability correction function is formulated as follows, based on Allen, 2007:

For **L < 0**

$$\Psi_{(m)}(200\text{m}) = 2\ \text{In}\left(\frac{1+x_{(200\ \text{m})}}{2}\right) + \text{In}\left(\frac{1+x^2_{(200\ \text{m})}}{2}\right) - 2\arctan\left(x_{(200\ \text{m})}\right) + 0.5\,\pi \quad \textbf{(6)}$$

$$\Psi_{(h)}(2\ \text{m}) = 2\ \text{In}\left(\frac{1+x^2_{(2\ \text{m})}}{2}\right) \quad \textbf{(7a)}$$

$$\Psi_{(h)}(0.1\ \text{m}) = 2\ \text{In}\left(\frac{1+x^2_{(0.1\ \text{m})}}{2}\right) \quad \textbf{(7b)}$$

Where,

$$x_{(200\ \text{m})} = \left(1 - 16\frac{200}{L}\right)^{0.25} \quad \textbf{(8a)}$$

$$x_{(2\ \text{m})} = \left(1 - 16\frac{2}{L}\right)^{0.25} \quad \textbf{(8b)}$$

$$x_{(0.1\ \text{m})} = \left(1 - 16\frac{0.1}{L}\right)^{0.25} \quad \textbf{(8c)}$$

Values for x_{200m}, x_{2m}, and $x_{0.1m}$ have no meaning when atmosphere is stable condition (L > 0), and their values are set to 1.0.

For L > 0

$$\Psi_{(m)}(200\text{m}) = -5\left(\frac{2}{L}\right) \quad \textbf{(9)}$$

$$\Psi_{(h)}(2\ \text{m}) = -5\left(\frac{2}{L}\right) \quad \textbf{(10a)}$$

$$\Psi_{(h)}(0.1\ \text{m}) = -5\left(\frac{0.1}{L}\right) \quad \textbf{(10b)}$$

When L=0, stability values are considered zero. In Equation 8, a height of 2 m is used instead of 200 m for z because, under stable conditions, the stable inertial boundary layer is expected to be only a few meters high. Using a height greater than 2 m may introduce numerical instability in the model. In neutral conditions, where L=0, the H is zero, and both Ψ_m and Ψ_h are also zero.

The SEBAL model determines dT for each pixel using a linear equation (dT = a + b × LST), where the coefficients a and b are derived by selecting two extreme temperature pixels—hot and cold pixels (Waters, 2002). The value of dT is updated during each iteration when computing correction parameters for the corrected aerodynamic resistance. The cold pixel represents a well-irrigated agricultural area characterized by low LST, high NDVI, and low surface albedo. It is assumed that in this region, all available energy is utilized for evapotranspiration, meaning LE is equal to Rn minus soil heat flux (LE = Rn - G) and H is negligible (H = 0). Consequently, the dT value at the cold pixel is expected to be close to zero, except in semi-arid and arid regions. The recommended approach for selecting the cold pixel involves choosing a well-watered agricultural field with healthy crop growth (Mkhwanazi *et al.,* 2015).

An optimal hot pixel is characterized by a significantly high temperature, indicating extreme dryness, where all available energy is used to heat the surface and the air above due to the lack of moisture for evaporation. This results in a high surface albedo (Mkhwanazi *et al.,* 2015). The selected pixel should ideally represent a bare surface with minimal biomass, indicated by a very low NDVI value. It is recommended to choose a dry agricultural area or bare soil while avoiding highways and buildings. The hot pixel is assumed to have zero LE and a large dT (Bastiaanssen *et al.,* 1998). These reference pixels serve as anchors for the calculations of all other pixels within the defined extreme conditions.

Evapotranspiration estimation: Using the instantaneous Rn, H, and G at the satellite overpass time, the instantaneous ET can be computed following Equation 10.

$$ET_i = \frac{\lambda ET}{\lambda} * 3600 \quad \textbf{(11)}$$

where ETi represents the instantaneous evapotranspiration (mm/hr), 3600 accounts for the conversion from seconds to hours, and λ is the latent heat of vaporization (J/kg), which corresponds to the energy required to convert water from liquid to vapor.

The Reference Evapotranspiration Fraction (ETrF) is calculated as the ratio of the estimated ETi for each pixel to the reference evapotranspiration (ETr) obtained from meteorological data:

$$ETrF = ETi / ETr \quad \textbf{(12)}$$

$$ET_{24} = ETrF * ETr\_24 \quad \textbf{(13)}$$

where; ETr_24 is the cumulative 24-hour ETr for the day of

the image.

4. Results

4.1 Spatiotemporal analysis of land surface heat fluxes in the study area

Satellite images from 27th October and 28th November 2022, 30th December 2022 and 31st January 2023, 16th February and 4th March 2023, and 21st April and 23rd May 2023 were selected to represent the autumn, winter, spring, and summer seasons, respectively. The visual representation of the spatiotemporal variations in land surface fluxes (Rn, H, G, and LE) retrieved from satellite data on the eight different dates are shown in Figure 2 and Figure 3.

To clearly illustrate the statistical distributions of these land surface heat fluxes, Table 2 presents their quartiles: Q1 (lower quartile), Q2 (median), and Q3 (upper quartile), which correspond to the 25%, 50%, and 75% positions in the distribution of values, respectively. The Rn values varied in descending order as summer > autumn > spring > winter, with their median values in these seasons being 607.7 W/m^2, 533.2 W/m^2, 521.6 W/m^2, and 459.9 W/m^2, respectively. Similarly, the G exhibited the same seasonal pattern, with median values of 113.2 Wm^{-2}, 91.0 W/m^2, 73.5 W/m^2, and 63.7 W/m^2 for summer, spring, autumn, and winter, respectively. In contrast, the seasonal variation in H followed a different pattern, decreasing in the order summer > winter > spring > autumn, with median values of 203.0 W/m^2, 71.6 W/m^2, 54.1 W/m^2, and 29.0 W/m^2, respectively. The LE, however, showed a substantial seasonal variation in descending order as autumn > spring > winter > summer, with median values of 427.3 W/m^2, 371.4 W/m^2, 322.2 W/m^2, and 289.3 W/m^2, respectively. Notably, the LE remained higher than the sensible heat flux across all seasons.

Table 2 Quartiles of land surface heat fluxes (Wm^{-2}) estimated by Landsat 8 data

	Dates	Quartiles	Net Radiation flux (R_n)	Ground heat flux (G)	Sensible heat flux (H)	Latent heat flux (LE)
Autumn	27/10/2022	Q1	551.08	71.47	17.99	346.18
		Q2	561.64	76.14	49.78	431.93
		Q3	571.28	81.46	118.65	475.90
	28/11/2022	Q1	491.84	67.05	0.26	385.44
		Q2	504.26	70.80	8.35	422.84
		Q3	515.29	73.87	30.24	443.92
Winter	30/12/2022	Q1	456.11	60.45	19.73	265.87
		Q2	468.35	62.47	59.80	340.71
		Q3	478.77	64.80	120.76	390.88
	31/01/2023	Q1	447.93	63.66	36.42	233.57
		Q2	456.01	64.87	83.55	303.84
		Q3	463.78	66.15	150.44	357.11
Spring	16/02/2023	Q1	495.14	85.02	48.99	275.42
		Q2	516.68	88.85	82.72	339.30
		Q3	535.08	91.99	127.87	394.20
	04/03/2023	Q1	512.86	90.71	4.54	344.15
		Q2	526.49	93.04	25.66	403.58
		Q3	538.31	95.59	66.82	438.84
Summer	21/04/2023	Q1	584.57	107.76	134.33	88.33
		Q2	610.41	114.07	239.29	255.90
		Q3	633.09	118.81	376.66	380.20
	24/05/2023	Q1	581.51	106.32	87.47	188.94
		Q2	604.98	112.35	166.55	322.74
		Q3	625.82	116.96	276.70	420.46

4.2 Spatiotemporal variation in land surface heat fluxes across four LULC classes

The Table 3 presents the temporal variation in land surface fluxes across four LULC classes: Open Water, Sugarcane Field, Deciduous Forest, and Orchard. Figure 4 and Figure 5 provide a visual representation of the

spatiotemporal variations in land surface energy fluxes across four LULC classes—crop fields, water bodies, urban areas, and orchards—for the autumn and winter seasons, as well as the spring and summer seasons, respectively. The selection of the four LULC classes in this study was based on their relevance to the objectives and conditions of the study area. Sugarcane and orchards are major cultivated areas with high water demand, while deciduous forests represent natural vegetation. Open water bodies serve as reference surfaces for maximum ET in the SEBAL model. These classes had well-defined, homogenous patches, and high spatial coverage. Other classes were excluded due to limited area coverage.

In autumn, open water exhibited the highest Rn values, ranging from 583.6 to 640.2 W/m^2 (Table 3), with a significant portion allocated to LE, highlighting active evaporation, while H was negligible. Sugarcane Fields showed a balanced energy distribution, with maximum LE reaching 389.2 W/m^2, indicating robust evapotranspiration during this period. Deciduous Forest exhibited minimal heat flux in autumn, with LE dominating, suggesting limited energy conversion into sensible heat. Similarly, Orchards followed a similar trend, with Rn primarily partitioned into LE, reflecting their evapotranspiration efficiency.

Table 3 Spatiotemporal variation in land surface heat fluxes across four LULC classes

LULC Classes			Open Water				Sugarcane Field				Deciduous Forest				Orchard			
	Dates	Values	Rn	G	H	LE	Rn	G	H	LE	Rn	G	H	LE	Rn	G	H	LE
Autumn	27/10/2022	Min	569.9	79.4	0	181.8	530.8	79.2	150.3	245.9	578.5	55.5	0	516.4	554.8	59.5	2.70	392.2
		Max	653.5	326.5	18.7	552.6	549.7	86.3	217.1	313.7	633.8	77.3	0	562.0	590.3	76.4	101.7	514.4
		Mean	640.2	313.4	0.92	325.6	540.5	81.6	174.3	284.4	601.0	64.0	0	537.2	573.3	66.8	24.3	482.1
	28/11/2022	Min	509.8	67.3	0	264.5	480.3	73.1	22.0	371.7	518.9	47.9	0	464.2	497.3	53.8	0	408.5
		Max	598.6	299.7	0.72	461.6	510.1	76.3	48.6	410.3	590.7	65.5	0	526.3	533.6	72.0	0	470.5
		Mean	583.6	280.4	0	303.6	494.2	74.8	30.1	389.2	548.8	56.1	0	493.2	516.0	61.9	0	454.6
Winter	30/12/2022	Min	476.8	59.4	0	238.4	451.4	62.0	74.2	309.3	467.1	45.8	0	402.7	468.2	49.6	0	285.0
		Max	554.9	277.8	0	429.7	465.4	65.2	90.8	318.2	549.6	60.3	20.3	492.1	500.0	63.9	119.3	441.8
		Mean	539.9	269.5	0	270.2	458.2	64.0	81.6	312.2	511.5	53.2	0.11	458.4	485.6	49.6	2.17	428.2
	31/01/2023	Min	455.3	59.9	0	235.6	441.0	65.0	105.7	239.5	458.9	60.3	0	310.3	457.4	59.9	0	314.2
		Max	524.4	262.2	0	446.4	450.0	65.4	135.9	279.3	502.6	64.9	85.4	439.7	480.6	64.8	82.6	420.6
		Mean	514.1	248.9	0	271.3	446.1	65.2	118.3	262.5	486.9	62.1	6.1	418.6	469.9	61.1	1.46	407.3
Spring	16/02/2023	Min	547.0	93.0	0	274.4	485.8	85.1	86.3	301.5	470.3	68.3	0.71	243.1	524.5	66.9	9.19	384.3
		Max	652.8	326.5	0	526.7	512.9	90.2	95.0	337.1	601.2	92.0	140.1	519.9	580.2	85.3	70.7	488.1
		Mean	638.0	311.0	0	321.4	499.9	88.4	92.0	319.5	564.4	80.2	23.1	460.9	557.1	74.5	19.8	461.2
	04/03/2023	Min	549.6	82.6	0	278.9	512.3	90.6	3.0	412.5	488.8	86.7	0	225.9	539.8	83.8	0	452.2
		Max	620.9	310.4	0	520.3	536.1	91.1	8.7	442.1	576.0	98.8	164.2	488.8	572.8	89.5	0.87	486.5
		Mean	607.8	299.8	0	308.4	527.8	90.8	5.3	431.6	550.8	91.4	16.9	442.4	555.8	86.4	0	469.5
Summer	21/04/2023	Min	597.3	102.2	0	256.4	568.4	114.0	315.3	50.8	549.1	94.1	47.5	0	619.4	84.1	24.25	357.6
		Max	741.1	370.5	202.8	613.8	606.2	119.4	399.2	177.0	676.8	124.8	575.8	519.1	692.4	110.4	170.3	559.7
		Mean	700.8	340.1	3.04	357.8	590.3	117.8	362.0	110.4	628.8	112.1	183.5	333.0	663.5	97.6	63.52	502.4
	24/05/2023	Min	572.3	101.1	0	170.2	624.3	105.6	59.8	368.4	558.8	86.5	11.5	138.3	464.2	82.2	0	370.0
		Max	727.1	363.3	285.3	602.8	640.0	114.5	153.2	474.5	667.2	120.0	322.2	559.2	728.6	107.1	122.4	625.7
		Mean	653.6	252.3	29.7	371.8	634.4	110.0	59.4	420.8	630.4	107.8	102.6	419.8	656.8	82.2	15.32	546.3

In winter, Open Water maintained lower Rn values, with G and LE dominating, while H was absent. Sugarcane Fields exhibited reduced energy partitioning to H and increased LE, with a maximum of 318.2 W/m^2 (Table 3), indicating the importance of moisture availability in winter. Deciduous Forest displayed minimal H, with a strong dominance of LE, reinforcing its role in moderating the microclimate. Orchards followed a similar pattern, with negligible H and high LE, reflecting their consistent water regulation

During spring, all LULC classes demonstrated an increase in Rn, with Open Water and Deciduous Forest showing maximum energy allocation to LE, while Sugarcane Fields displayed a balance between H and LE, reflecting active crop growth. Orchards maintained relatively high LE, indicating continued evapotranspiration despite increasing temperatures.

In summer, Open Water recorded the highest Rn values, exceeding 700 W/m^2, with G and LE dominating, while H contributions were minor. Sugarcane Fields experienced significant energy partitioning into LE, with a maximum value of 474.5 W/m^2 (Table 3), indicating high moisture demand and evapotranspiration under peak temperatures. Deciduous Forest showed moderate energy

allocation to LE, reflecting its resilience to summer heat, while Orchards exhibited an increase in H and LE, suggesting active physiological processes to cope with elevated temperatures.

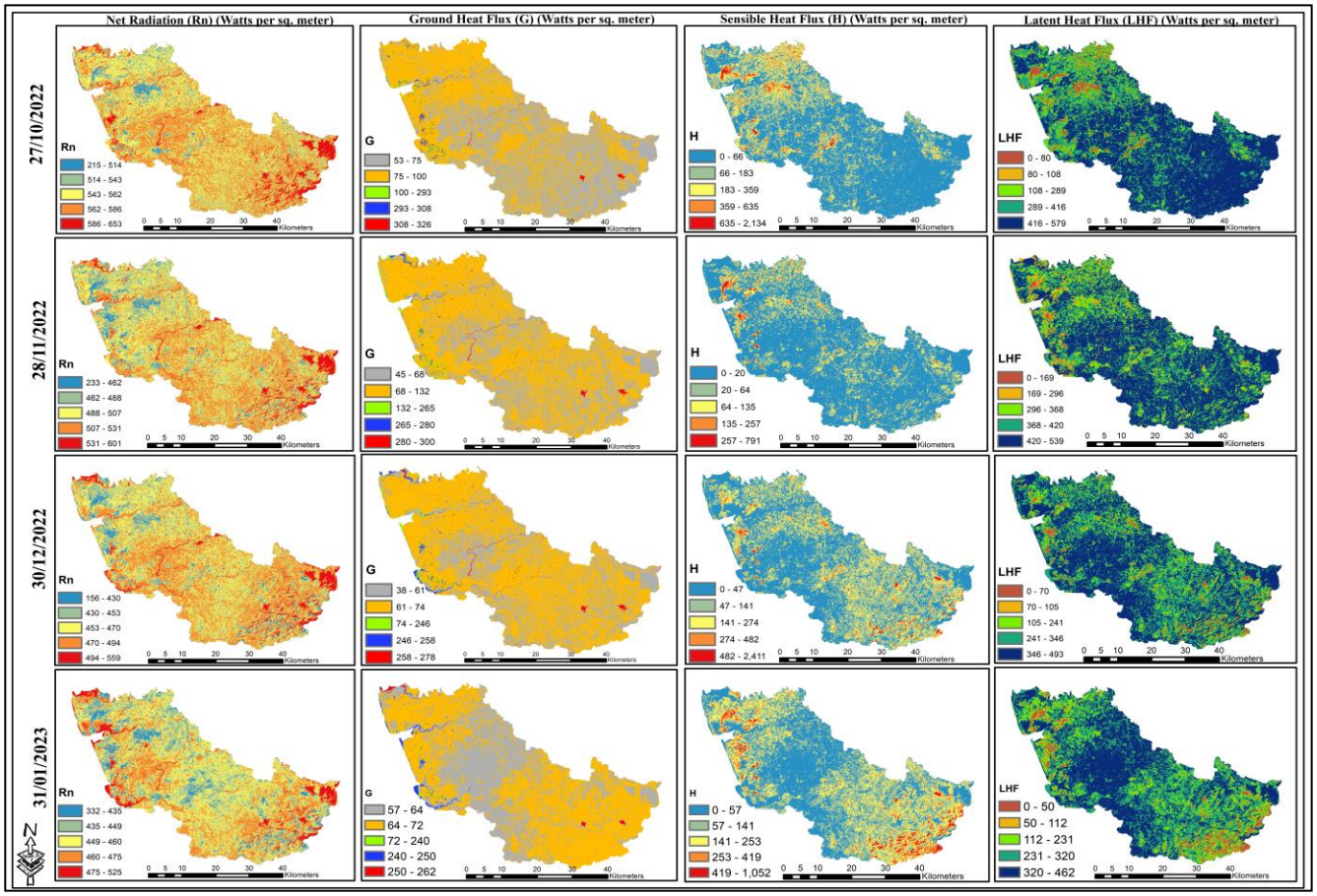

Fig. 2. Spatiotemporal distributions of land surface heat fluxes for the autumn and winter season

4.3 Interdependence of SEBAL model outputs

The SEBAL model estimates various land surface fluxes, which exhibit interdependence. The coefficient of determination (R^2) between Rn and SEBAL-estimated ET was found to be 0.68 (Figure 6a), indicating a moderate dependency of ET on net radiation. This suggests that Rn plays a significant role in driving ET, as it provides the primary energy input required for evaporation and transpiration processes. A stronger relationship was observed between G and LST, with an R^2 value of 0.70 (Figure 6b). This indicates that G is influenced by LST, as higher LST results in increased G due to heat transfer into the ground surface layers, impacting the overall energy balance (Figure 6b). Crago *et al.,* (2014) emphasized that LST serves as an important boundary

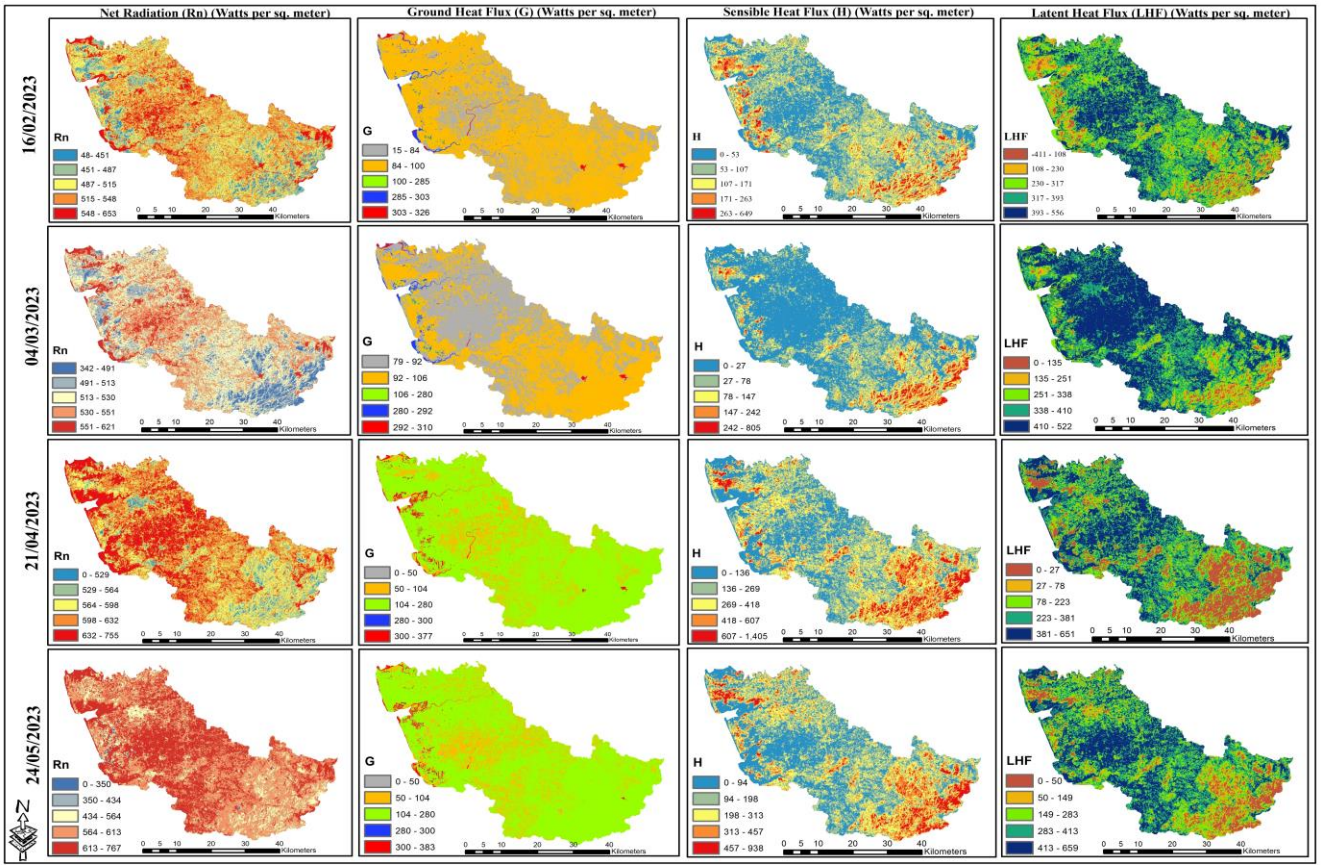

Fig. 3. Spatiotemporal distributions of land surface heat fluxes for the spring and summer seasons.

condition for the fluxes of H and water vapor (ET) into the atmosphere, as well as for G into the ground.

The relationship between ET and G (Figure 6c) also highlights a strong interdependence, with an R^2 value of 0.70, suggesting that ET is significantly influenced by G. This correlation indicates that the vertical movement of water within the soil is affected by G, leading to increased ET rates under higher soil heat conditions. The strongest correlation ($R^2 = 0.95$) was observed between SEBAL-estimated ET and H (Figure 6d), emphasizing the model high accuracy in predicting ET based on H estimation. However, the accuracy of H estimation is highly dependent on the selection of hot and cold pixels, which significantly influences the results. To improve H estimation, advanced methods for selecting hot and cold pixels have been developed by researchers such as Ma *et al.,* (2023), Saboori *et al.,* (2021), and Kisekka *et al.,* (2024).

Furthermore, an R^2 value of 0.87 between SEBAL-estimated ET and the L (Figure 6e) indicates a strong correlation, demonstrating the model ability to capture the relationship between atmospheric stability and ET. Under stable atmospheric conditions, energy exchange between the surface and the atmosphere is restricted, resulting in lower ET rates. In contrast, unstable conditions promote enhanced mixing, leading to higher ET rates (Hussein, 2019). In neutral atmospheric conditions, where vertical mixing is minimal, ET rates remain moderate. By incorporating L, the SEBAL model ensures a more precise estimation of ET under different atmospheric states. These findings align with previous studies by Massmann *et al.,* (2019), which highlight the role of atmospheric stability in governing ET rates. Additionally, a high R^2 value of 0.95 between H and r_{ah} ((Figure 6f) confirms that H is strongly dependent on r_{ah} calculations. Mohan *et al.,* (2020) emphasized that H estimation is highly sensitive to r_{ah}, affecting the accuracy of energy flux predictions. Moreover, an R^2 value of 0.96 between H and ET (Figure 6d) underscores the direct influence of r_{ah} on ET estimation, demonstrating the interlinked nature of H, r_{ah}, and ET in surface energy balance computations. Stability corrections, based on Monin-Obukhov similarity theory, are often applied iteratively to refine r_{ah} calculations, ensuring accurate representation of atmospheric conditions.

Overall, the strong interdependence among SEBAL-estimated fluxes—particularly ET, Rn, G, H, r_{ah}, and L—highlights the necessity of accurate input data and parameter selection to ensure robust SEBAL model performance in land surface energy balance studies.

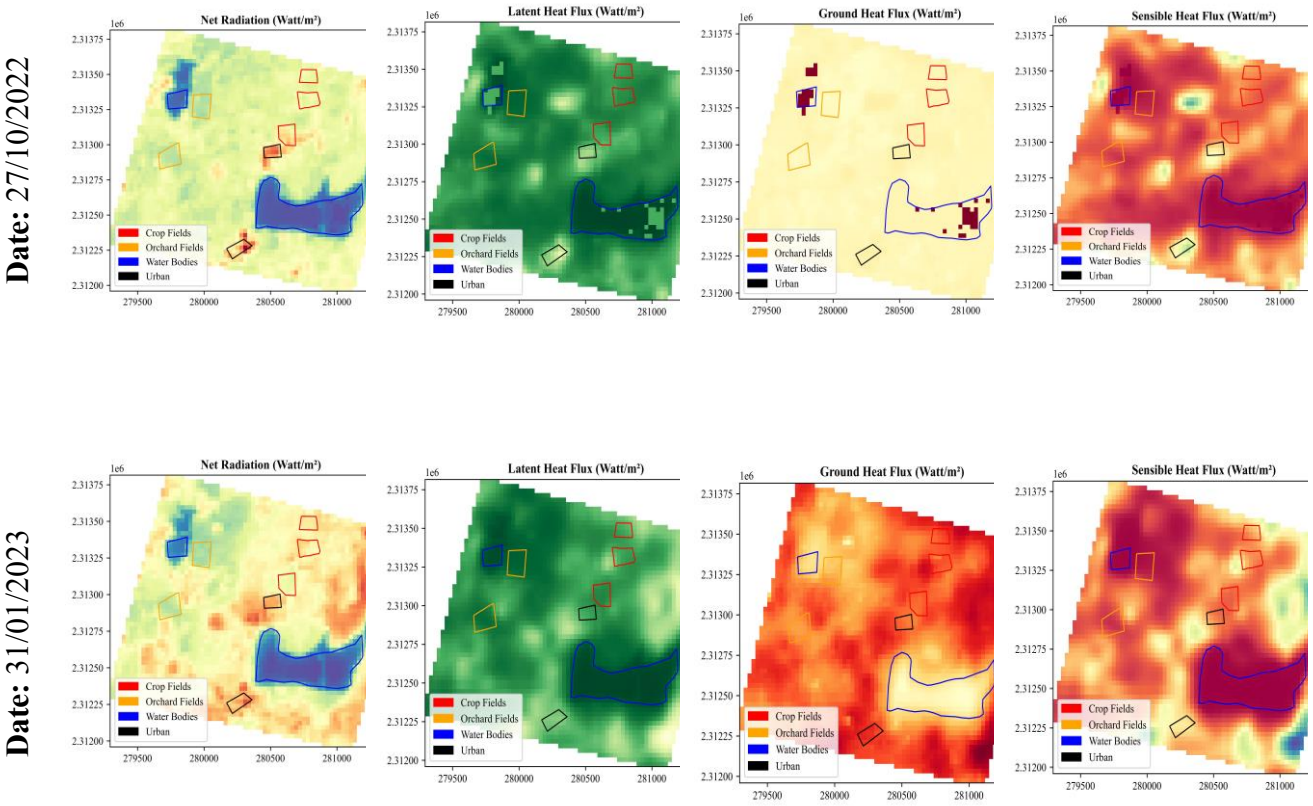

Fig. 7. Visual representation of spatiotemporal variation in land surface energy fluxes across four LULC classes for autumn and winter seasons.

5 Discussion

The seasonal variations in energy fluxes are primarily driven by fluctuations in solar radiation, land surface properties, and atmospheric conditions. Changes in the solar angle and day length across seasons significantly impact Rn, which subsequently affects the distribution of energy among H, LE, and G. The seasonal variations in energy fluxes are governed by the distinct characteristics of the LULC classes. Open Water exhibited the highest latent heat flux throughout the seasons, indicating dominant evaporative processes, while G values were significant, reflecting heat storage capacity. Sugarcane fields demonstrated moderate LE values, with a balanced partitioning between H and G. Deciduous forests showed high LE during autumn and spring, reflecting active transpiration, while H remained negligible. Orchards displayed notable LE values, particularly during spring and summer, with increased H in the summer due to enhanced heat transfer. The variability in energy fluxes underscores the influence of vegetation type, soil properties, and atmospheric conditions on the energy balance. These findings provide critical insights for water resource management and irrigation planning, particularly in areas dominated by agricultural and forested landscapes.

Due to the lack of ground-based flux measurement instruments, such as an eddy covariance tower, real flux measurements could not be obtained in the study area. However, previous studies by Bala *et al.,* (2016); Rawat *et al.,* (2017); Sawadogo *et al.,* (2020) and Baboli *et al.,* (2024) compared SEBAL-derived ET with lysimeter data and reported R^2 values of 0.91, 0.85, 0.73, and 0.94, respectively. Peddinti *et al.,* (2024) compared SEBAL fluxes with eddy covariance flux tower measurements, achieving strong accuracy with RMSE values of 33 W/m^2 (12%) for latent heat flux, 29 W/m^2 (35%) for sensible heat flux, 24 W/m^2 for net radiation, 10 W/m^2 for soil heat flux, and 0.26 mm/day

for ET estimates. These findings underscore the SEBAL model reliable accuracy when compared with ground-based

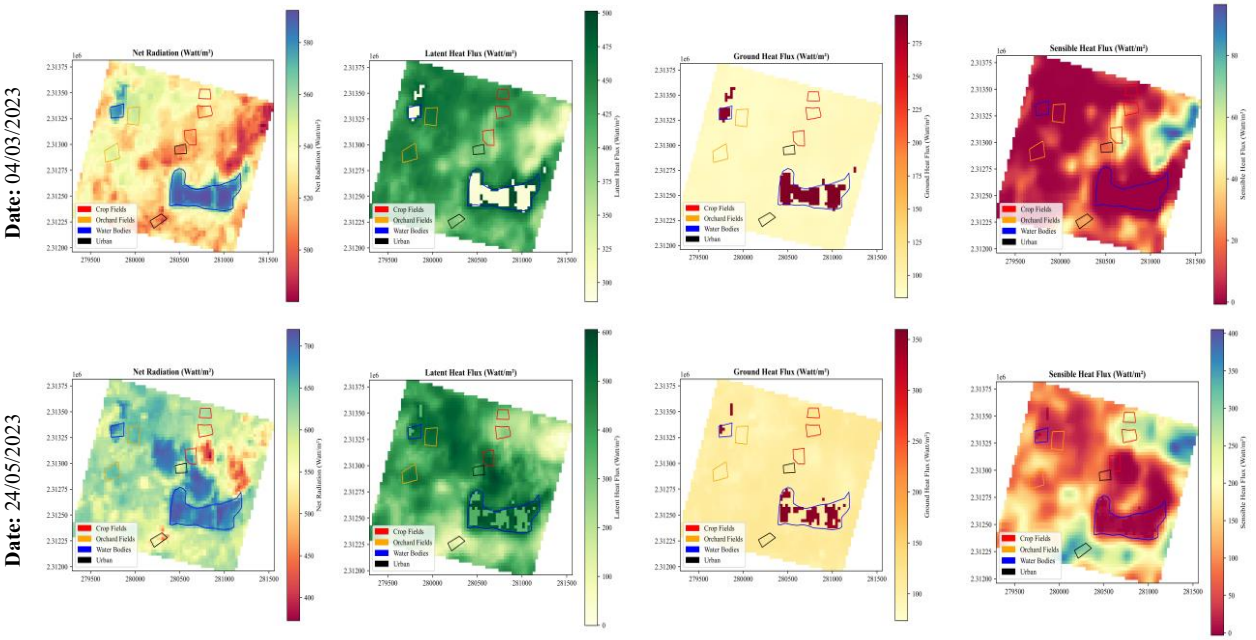

Fig 5: Visual representation of spatiotemporal variation in land surface energy fluxes across four LULC classes for spring and summer seasons

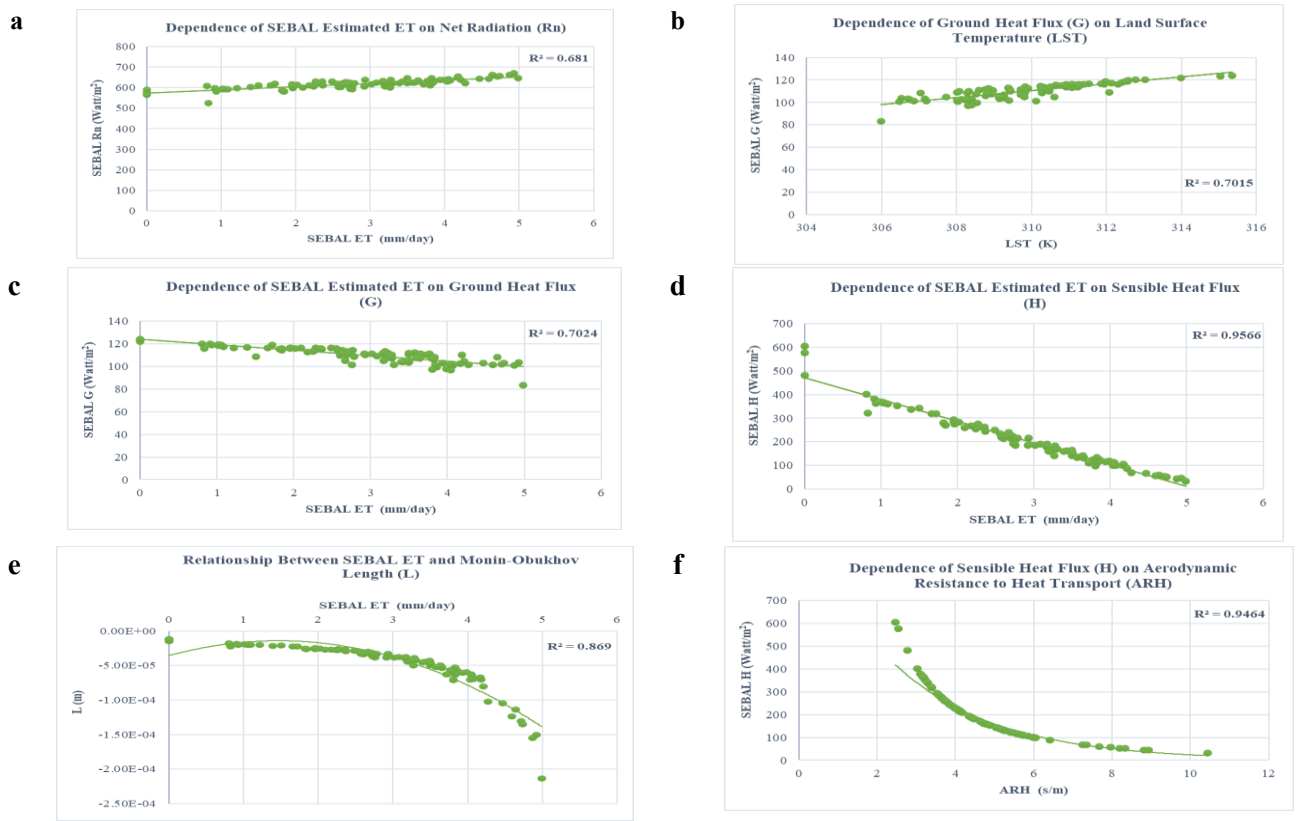

Fig. 6. Interdependence of SEBAL model outputs: (a) ET on Rn, (b) G on LST, (c) ET on G, (d) ET on H, (e) ET on L, and (f) H on ARH

observational systems, making it a robust tool for fluxes estimation, particularly in regions lacking such observational systems.

The SEBAL model serves as a reliable tool for estimating energy fluxes, particularly in regions where micrometeorological instruments, such as eddy covariance systems, are unavailable and where lysimeter facilities for direct AET measurements are lacking. In this study, SEBAL was chosen over the TSEB model due to the absence of micrometeorological observation facilities, which are essential for providing the input data required by TSEB. The accuracy and applicability of the SEBAL model are influenced by several limitations. Complex terrain and diverse surface characteristics in the study area pose challenges in accurately representing energy and heat exchanges between the land surface and the atmosphere. Parameter calibration during SEBAL model setup can introduce errors, particularly if performed subjectively, affecting overall model precision. A crucial step in the process is the selection of 'cold' and 'hot' pixels, which can impact model reliability (Wang *et al.,* 2014; Mhawej *et al.,* 2020; Ma *et al.,* 2023). Additionally, under advective conditions, especially in arid and semi-arid regions, SEBAL may underestimate ET due to its limited consideration of advection effects (Allen *et al.,* 2005). Cloud cover presents another challenge, as even thin layers can disrupt radiation energy calculations, leading to potential inaccuracies (Shamloo *et al.,* 2021). Implementing the SEBAL model is highly data-intensive, requiring multiple inputs such as land surface temperature, vegetation indices, and surface albedo, which can be difficult to acquire and process efficiently (Nikfal and Karimi, 2024). Additionally, surface heating can induce instability in the lower atmosphere, complicating the estimation of thermodynamic r_{ah} and dT. Since these parameters require at least five iterative computations for accurate refinement (Ma *et al.,* 2023), determining H remains particularly challenging.

6.1 Limitation and future scope

Landsat 8 satellite data, with their high spatial resolution (30m), effectively capture the spatial distribution of H and LE. However, their limitations, including long revisit intervals and low temporal resolution (16 days), make it challenging to accurately analyze diurnal variations. Additionally, a significant portion of Landsat 8 images exhibit high mean cloud cover, potentially leading to substantial errors in land surface energy flux estimations. In addition to these sensor-related constraints, several region-specific factors in Navsari may also affect the accuracy of SEBAL outputs. The district's coastal location leads to high humidity and frequent sea breeze circulation, which influence atmospheric stability and can impact the estimation of sensible heat flux (Bastiaanssen *et al.,* 1998). The presence of mixed cropping systems, orchards, and fragmented landholdings creates a heterogeneous landscape in terms of canopy structure and surface roughness, thereby complicating key assumptions of the SEBAL model (Gowda *et al.,* 2008).

Future advancements hold great potential for enhancing the accuracy and usability of the SEBAL model. Incorporating data from emerging satellite missions, such as Sentinel-2 and Landsat 9, can provide improved spatial and temporal resolution, leading to more precise AET estimations, particularly for regions requiring detailed crop monitoring. Additionally, refining cloud masking and gap-filling methods would enhance the model's effectiveness in areas frequently affected by cloud cover (Lu *et al.,* 2021). Automating the selection of hot and cold pixels within the model streamlines the process by identifying extreme temperature pixels without manual intervention, making it more efficient and time-saving (Gao *et al.,* 2011; Bhattarai *et al.,* 2017).

6. Conclusion

Landsat 8 data based SEBAL model has demonstrated its capability in estimating AET, LST, albedo, NDVI, crop coefficient, and various energy fluxes (Rn, LE, H, and G) across large and heterogeneous landscapes. One of the key advantages of this remote sensing-based approach is its cost-effectiveness and its ability to capture spatial variability at multiple scales, providing valuable insights into surface energy balance processes. However, its accuracy is influenced by factors such as cloud cover, land surface characteristics, and the selection of hot and cold pixels. Seasonal variations in solar radiation, atmospheric conditions, and land cover further impact the distribution of energy fluxes, necessitating careful consideration in energy balance modeling.

SEBAL proves to be a reliable tool for monitoring surface energy balance fluxes, particularly in regions lacking ground-based observational networks such as eddy covariance flux towers. However, its reliability may vary depending on seasonal conditions, land use/land cover complexity, and the need for region-specific calibration, especially in mixed-irrigation agricultural systems. Therefore, results should be interpreted with caution in physio graphically diverse landscapes, and where possible, supported by local ground validation.

Additionally, its capacity to estimate AET is particularly significant in areas without lysimeter facilities, supporting improved assessments of crop water requirements and facilitating precise irrigation scheduling. This study highlights the effectiveness of the SEBAL model in assessing the spatiotemporal variations of land surface

fluxes across the study area, including LULC-based analysis. Additionally, the study evaluates actual sugarcane water requirements using both the SEBAL and METRIC EEFlux models. Future research should focus on developing energy balance model algorithms that are compatible with multiple satellite datasets, allowing for improved temporal resolution and seamless integration of diverse remote sensing inputs. These efforts will enhance the reliability of SEBAL-derived energy flux estimates, making it a more effective tool for large-scale hydrological and agricultural studies.

Acknowledgments

Author acknowledges the providers of Landsat 8 data and the developers of GRASS GIS software for their indirectly contributions to geospatial analysis. Finally, author express our gratitude to our families and peers for their continuous support and encouragement throughout this research.

Declarations

Author contributions

V. B. Virani: Conceptualization, Writing – original draft, Methodology, Visualization, Software, Data curation.

Funding Statement

This research was conducted without external financial support, reflecting the independent efforts and commitment of the authors.

Data Availability

The datasets generated and/or analysed during the current study are available in a publicly accessible repository.

Competing Interests

The authors have no relevant financial or non-financial interests to disclose.

References

Allen, R.G., Tasumi, M., & Morse, A. (2005). A Landsat-based energy balance and evapotranspiration model in Western US water rights regulation and planning. *Irrigation and Drainage Systems*, *19*(3-4), 251–268.

Allen, R.G., Tasumi, M., & Trezza, R. (2007). Satellite-based energy balance for mapping evapotranspiration with internalized calibration (METRIC)—Model. *Journal of Irrigation and Drainage Engineering*, *133*(4), 380–394.

Aryalekshmi, B.N., Biradar, R.C., Chandrasekar, K., & Ahamed, J.M. (2021). Analysis of various surface energy balance models for evapotranspiration estimation using satellite data. *Egyptian Journal of Remote Sensing and Space Science*, *24*(3), 1119–1126.

Baboli, N., Ghamarnia, H., & Hafezparast Mavaddat, M. (2024). Estimating wheat evapotranspiration through remote sensing utilizing GeeSEBAL and comparing with lysimetric data. *Applied Water Science*, *14*, 193.

Bala, A., Rawat, K.S., Misra, A.K., & Srivastava, A. (2016). Assessment and validation of evapotranspiration using SEBAL algorithm and lysimeter data of IARI agricultural farm, India. *Geocarto International*, *31*(7), 739–764.

Bastiaanssen, W.G.M. (2000). SEBAL-based sensible and latent heat fluxes in the irrigated Gediz Basin, Turkey. *Journal of Hydrology*, *229*(1-2), 87–100.

Bastiaanssen, W.G.M., Pelgrum, H., Wang, J., Ma, Y., Moreno, J., Roerink, G., & Van der Wal, T. (1998). A remote sensing surface energy balance algorithm for land (SEBAL): Part 2: Validation. *Journal of Hydrology*, *212-213*, 213–229.

Beg, A.A.F., Al-Sulttani, A.H., Ochtyra, A., Jarocińska, A., & Marcinkowska, A. (2016). Estimation of evapotranspiration using SEBAL algorithm and Landsat-8 data—A case study: Tatra Mountains region. *Journal of Geological Research and Engineering*, *6*(3), 257–270.

Bhattacharya, B.K., Mallick, K., Desai, D., Bhat, G.S., Morrison, R., Clevery, J.R., & Baldocchi, D. (2022). A coupled ground heat flux–surface energy balance model of evaporation using thermal remote sensing observations. *Biogeosciences*, *19*(24), 5521–5551.

Bhattarai, N., Quackenbush, L.J., Im, J., & Shaw, S.B. (2017). A new optimized algorithm for automating endmember pixel selection in the SEBAL and METRIC models. *Remote Sensing of Environment*, *196*, 178–192.

Caiserman, A., Amiraslani, F., & Dumas, D. (2021). Assessment of the agricultural water budget in southern Iran using Sentinel-2 to Landsat-8 datasets. *Journal of Arid Environments*, *188*, 104461.

Filgueiras, R., Mantovani, E.C., Althoff, D., Ribeiro, R.B., Venancio, L.P., & dos Santos, R.A. (2019). Dynamics of actual crop evapotranspiration based in the comparative analysis of SEBAL and METRIC-eeflux. *Irrigation*, *1*, 72–80.

Gao, Z.Q., Liu, C.S., Gao, W., & Chang, N.B. (2011). A coupled remote sensing and the Surface Energy Balance with Topography Algorithm (SEBTA) to estimate actual evapotranspiration over

heterogeneous terrain. *Hydrology and Earth System Sciences*, *15*(1), 119–139.

Gowda, P.H., Chavez, J.L., Colaizzi, P.D., Evett, S.R., Howell, T.A., & Tolk, J.A. (2008). ET mapping for agricultural water management: present status and challenges. *Irrigation science*, *26*, 223-237.

Hussein, M.M. (2019). Impact of atmospheric stability conditions on heat fluxes from Alexandria Eastern Harbor, Egypt. *Egyptian Journal of Aquatic Research*, *45*(4), 313–319.

Inman-Bamber, N.G. (1991). Growth model for sugarcane based on a simple carbon balance and the CERES-Maize water balance. *South African Journal of Plant and Soil*, *8*(2), 93–99.

Karishma, C.G., Kannan, B., Nagarajan, K., Panneerselvam, S., & Pazhanivelan, S. (2022). Spatial and temporal estimation of actual evapotranspiration of lower Bhavani basin, Tamil Nadu using Surface Energy Balance Algorithm for Land Model. *Journal of Applied and Natural Science*, *14*(2), 566.

Kisekka, I., Ghorbanpour, A., Peddinti, S.R., Hessels, T., & Bastiaanssen, W. (2024). Advanced sensible heat flux range determination in composite terrain through innovative optimization of hot and cold pixels for enhanced accuracy. SSRN, 4886805.

Lawrence, D., & Vandecar, K. (2015). Effects of tropical deforestation on climate and agriculture. *Nature Climate Change*, *5*(1), 27–36.

Lu, S., He, M., He, S., Pan, Y., Yin, W., & Li, P. (2021). An improved cloud masking method for GOCI data over turbid coastal waters. *Remote Sensing*, *13*(14), 2722.

Ma, Y., Sun, S., Li, C., Zhao, J., Li, Z., & Jia, C. (2023). Estimation of regional actual evapotranspiration based on the improved SEBAL model. *Journal of Hydrology*, *619*, 129283.

Massmann, A., Gentine, P., & Lin, C. (2019). When does vapor pressure deficit drive or reduce evapotranspiration? *Journal of Advances in Modeling Earth Systems*, *11*(10), 3305–3320.

McShane, R.R., Driscoll, K.P., & Sando, R. (2017). A review of surface energy balance models for estimating actual evapotranspiration with remote sensing at high spatiotemporal resolution over large extents. *Scientific Investigations Report*, 2017(5087).

Mhawej, M., Caiserman, A., Nasrallah, A., Dawi, A., Bachour, R., & Faour, G. (2020). Automated evapotranspiration retrieval model with missing soil-related datasets: The proposal of SEBALI. *Agricultural Water Management*, *229*, 105938.

Mkhwanazi, M., Chávez, J.L., & Andales, A.A. (2015). SEBAL-A: A remote sensing ET algorithm that accounts for advection with limited data. Part I: Development and validation. *Remote Sensing*, *7*, 15046–15067.

Mohan, M.P., Kanchirapuzha, R., & Varma, M.R. (2020). Review of approaches for the estimation of sensible heat flux in remote sensing-based evapotranspiration models. *Journal of Applied Remote Sensing*, *14*(041501).

Nikfal, A., & Karimi, M.A. (2024). Operational workflow to simulate biophysical variables, based on the coupled WRF/SEBAL models. *Computers and Electronics in Agriculture*, *222*, 109003.

Norman, J.M., Kustas, W.P., & Humes, K.S. (1995). A two-source approach for estimating soil and vegetation energy fluxes in observations of directional radiometric surface temperature. *Agricultural and Forest Meteorology*, *77*, 263–293.

Paulson, C.A. (1970). The mathematical representation of wind speed and temperature profiles in the unstable atmospheric surface layer. *Journal of Applied Meteorology*, *9*, 857–861.

Peddinti, S.R., Nicolas, F., Raij-Hoffman, I., & Kisekka, I. (2024). Evapotranspiration estimation using high-resolution aerial imagery and pySEBAL for processing tomatoes. *Irrigation Science*, 1–14.

Peng, S., Piao, S., Ciais, P., Friedlingstein, P., Ottle, C., Bréon, F.M., & Myneni, R.B. (2012). Surface urban heat island across 419 global big cities. *Environmental Science & Technology*, *46*, 696–703.

Rawat, K.S., Bala, A., Singh, S.K., & Pal, R.K. (2017). Quantification of wheat crop evapotranspiration and mapping: A case study from Bhiwani District of Haryana, India. *Agricultural Water Management*, *187*, 200–209.

Saboori, M., Mokhtari, A., Afrasiabian, Y., Daccache, A., Alaghmand, S., & Mousivand, Y. (2021). Automatically selecting hot and cold pixels for satellite actual evapotranspiration estimation under different topographic and climatic conditions. *Agricultural Water Management*, *248*, 106763.

Sawadogo, A., Hessels, T.I.M., Gündoğdu, K.S., Demir, A.O., Mustafa, Ü.N.L.Ü., & Zwart, S.J. (2020). Comparative analysis of the pySEBAL model and lysimeter for estimating actual evapotranspiration of soybean crop in Adana, Turkey. *International Journal of Engineering and Geosciences*, *5*, 60–65.

Saxena, D., Choudhary, M., & Sharma, G. (2024). Spatiotemporal trends and evapotranspiration estimation using an improvised SEBAL convergence method for the semi-arid region of

Western Rajasthan, India. *AQUA—Water Infrastructure, Ecosystems, and Society*, *73*, 407–423.

Seneviratne, S.I., Corti, T., Davin, E.L., Hirschi, M., Jaeger, E.B., Lehner, I., & Teuling, A.J. (2010). Investigating soil moisture–climate interactions in a changing climate: A review. Earth-Science Reviews, *99*, 125–161.

Shamloo, N., Taghi Sattari, M., Apaydin, H., Valizadeh Kamran, K., & Prasad, R. (2021). Evapotranspiration estimation using SEBAL algorithm integrated with remote sensing and experimental methods. *International Journal of Digital Earth*, *14*, 1638–1658.

Shukla, G., Tiwari, P., Dugesar, V., & Srivastava, P.K. (2021). Estimation of evapotranspiration using surface energy balance system and satellite datasets. *Agricultural Water Management*, Academic Press, 157–183.

Silva, B.B.D., Braga, A.C., Braga, C.C., de Oliveira, L.M., Montenegro, S.M., & Barbosa Junior, B. (2016). Procedures for calculation of the albedo with OLI-Landsat 8 images: Application to the Brazilian semi-arid. Revista Brasileira de Engenharia Agrícola e Ambiental, *20*, 3–8.

Singh, R.K., Irmak, A., Irmak, S., & Martin, D.L. (2008). Application of SEBAL model for mapping evapotranspiration and estimating surface energy fluxes in south-central Nebraska. *Journal of Irrigation and Drainage Engineering*, *134*, 273–285.

Su, Z. (2002). The Surface Energy Balance System (SEBS) for estimation of turbulent heat fluxes. *Hydrology and Earth System Sciences*, *6*, 85–100.

Virani, V.B., Kumar, N., Mote, B.M., Chaudhari, N.M., & Delvadiya, J.B. (2024). Assessment of spatiotemporal variations in actual evapotranspiration using the pySEBAL model and remote sensing data in Navsari, Gujarat, India. *Mausam*, *75*, 943–954.

Wagle, P., Gowda, P.H., & Northup, B.K. (2019). Annual dynamics of carbon dioxide fluxes over a rainfed alfalfa field in the US Southern Great Plains. *Agricultural and Forest Meteorology*, *265*, 208–217.

Wang, K., Dickinson, R.E., Wild, M., & Liang, S. (2018). Evidence for decadal variation in global terrestrial evapotranspiration between 1982 and 2002: 1. Model development. *Journal of Geophysical Research: Atmospheres*, 113(D10).

Wang, X.G., Wang, W., Huang, D., Yong, B., & Chen, X. (2014). Modifying SEBAL model based on the trapezoidal relationship between land surface temperature and vegetation index for actual evapotranspiration estimation. *Remote Sensing*, *6*(7), 1–29.

Waters, R. (2002). Surface Energy Balance Algorithms for Land–Idaho Implementation. Waters Consulting and University of Idaho and WaterWatch Inc., Nelson, British Columbia.

Webb, E.K. (1970). Profile relationships: The log-linear range, and extension to strong stability. *Quarterly Journal of the Royal Meteorological Society*, *96*, 67–90.

Zhang, K., Kimball, J.S., & Running, S.W. (2016). A review of remote sensing-based actual evapotranspiration estimation. *Wiley Interdisciplinary Reviews: Water*, *3*(6), 834–853.

Zhang, X.C., Wu, J.W., Wu, H.Y., & Li, Y. (2011). Simplified SEBAL method for estimating vast areal evapotranspiration with MODIS data. *Water Science and Engineering*, *4*(1), 24–35.

Zhao, L., Lee, X., Smith, R.B., & Oleson, K. (2014). Strong contributions of local background climate to urban heat islands. *Nature*, *511*(7508), 216–219.